arXiv:astro-ph/0006156v1 12 Jun 2000

Interferometric observation of the L483 molecular core

Y.-S. Park[1,2,3], J.-F. Panis[4], N. Ohashi[1], M. Choi[1], and Y.C. Minh[2]

ABSTRACT

We present the aperture synthesis imaging of C_3H_2 2_{12}–1_{01} and HCO^+ 1–0 lines and of continuum emission at $\lambda = 3.4$ mm toward the class 0 young stellar object, IRAS 18148-0440 in the L483 molecular cloud. The continuum emission is detected at the IRAS position at a level of 16 mJy, indicating a compact source with a mass of $\sim 0.13 M_\odot$. The C_3H_2 delineates an envelope near the IRAS position, with a size of $\sim$ 3000 AU $\times$ 2000 AU in R.A. and Dec. directions, respectively. A velocity gradient detected only along the axis of outflow can be explained in terms of free-fall motion of the envelope. The HCO^+ line wing extends up to the velocity of ± 6 km s^{-1} relative to the systemic one, and the high velocity material shows a symmetric bipolarity and extends over $2'$ or 0.1 pc along the east-west direction. It is found that the outflow material is clumpy and the opening angle is widest for the slowest moving component. The core component of the HCO^+ 1–0 line exhibits an anti-infall asymmetry not only in interferometric but also in single dish observations. It is attributable to the slow isotropic outward motion of gas between the flattened envelope and the collimated outflow.

Subject headings:

1. Introduction

Young stellar objects (YSOs) in the early phase of star formation continuously aggregates material from parent dense molecular cores. This process seems to be followed by the formation of disk and outflows, and protostars come into existence by dispersing debris around them (Kitamura et al. 1997). This scenario is generally accepted at least for low mass stars. The classification or evolutionary sequence of YSOs from class 0 to III, mainly based on their spectral energy distribution, has been established and became a framework to which subsequent studies should refer (André, Ward-Thompson, & Barsony 1993).

[1]Institute of Astronomy and Astrophysics, Academia Sinica, P.O. Box 1-87, Nankang, Taipei, Taiwan 115, R.O.C.

[2]Korea Astronomy Observatory, San 36-1, Whaam-dong, Yusung, Taejon, 305-348, Korea

[3]Astronomy Program, SEES, Seoul National University, San 56-1, Shillim-dong, Kwanak-gu, Seoul, 151-742, Korea

[4]Radioastronomie, École Normal Supérieure, 24 rue Lhomond, 75231, Paris cedex 05, France

However, one needs to find direct observational evidence of inward motion leading to a drastic density enhancement of central source which is prerequisite for the star formation. The method of diagnosing the collapse motion had been developed earlier (Leung & Brown 1977; Anglada et al. 1987), but it was first detected only in the 1990's (Zhou et al. 1993). The method is based on the idea that, in the presence of the infall motion of which magnitude is not so large as that of intrinsic (turbulent + thermal) motion, an opaque line has a self-absorption with the blue peak stronger than the red one, while an optically thin line with a single peak is located between the two peaks of the opaque line. Since class 0 and I objects are believed to be in main accretion phase, prompt attention is paid to them in an attempt to understand the earliest phase of star forming process. Many class 0 and I sources have been surveyed initially with single dish telescopes mainly for the detection of infall signatures, resulting in a statistical preference for inward motion rather than outward one for these objects (Gregersen et al. 1997; Mardones et al. 1997). These surveys also served as a basis for detailed studies of higher angular resolution. Imaging with high spatial resolution is particularly important since the star formation process takes place at a smaller scale. Only interferometric observations enable us to separate envelopes, disks, and outflow lobes and to disentangle motions associated with them. Choi et al. (1999) carried out a survey of 9 class 0 sources using the Berkeley-Illinois-Maryland-Association (BIMA) interferometer, and Hogerheijde et al. (1999) on the YSOs in the Serpens molecular cloud. Detailed investigation has been undertaken for a limited number of YSOs as well (Ohashi et al. 1997; Yang et al. 1997). Eventually all YSOs will have to be observed with interferometers in a variety of transitions.

As a step toward these high resolution studies, we conducted an interferometric observation of L483. The L483 is one of the so-called Myers' cores containing an embedded infrared source, IRAS 18148-0440, at a distance of 200 pc. Its size is $\sim 1'$ from the observations of HC_3N (Fuller & Myers 1993) and $C^{18}O$ (Fuller & Ladd 1997). A CO outflow with a good collimation was found in the east-west direction, inclined by $\sim 45^\circ$ to the sky plane, and an infrared lobe also lies in the axis of molecular outflow (Parker, Padman, & Scott 1991; Fuller et al. 1995). Recently, Hatchell, Fuller, & Ladd (1999) and Buckle, Hatchell, & Fuller (1999) examined the temperature variation in the outflow lobe and the shock structure of jet embedded in the lobe, respectively. However, the kinematics of the central condensation remains poorly understood, since the line asymmetry of optically thick transitions, known as a probe of internal motions of cores, differs from molecule to molecule. Mardones et al. (1997) and Mardones (1998) obtained CS 2–1, H_2CO 2_{12}–1_{11}, and N_2H^+ 1–0 lines with $20'' \sim 30''$ beams and mapped their spatial distributions. They found that the CS and H_2CO lines are self-reversed and the blue peak is slightly brighter than the red. On the other hand, Gregersen et al. (1997) show that the red peak is twice as strong as the blue one in the HCO^+ 3–2 transition in a $\sim 20''$ beam. The three hyperfine components of HCN 1–0 again exhibit the usual blue asymmetry with a $\sim 60''$ beam: a single peak in the blue side with a shoulder in the red of the thinnest component (F=0–1) changes into a deep self-absorption with a stronger blue peak of the thickest one (F=2–1) (Park, Kim, & Minh 1999). A recent VLA observation of NH_3 indicates an inward motion down to $\sim 10''$ scale (Fuller & Wooten 2000). All these features suggest diverse velocity fields in this source, and this could be understood much

better by aperture synthesis imaging.

In section 2, we briefly describe the observation and the data reduction. Results of our interferometric observation are presented in section 3. In section 4, we discuss kinematics of the envelope and outflow as well as molecular abundance. In the final section, we summarize our results.

2. Observation and data reduction

Since the HCO^+ molecule is most peculiar in line shape when compared with other molecules in single dish observations, the HCO^+ molecule is the one to be explored with a prime importance in this observational study. The HCO^+ 1–0 transition has a critical density of $\sim 2.5 \times 10^5$ cm^{-3}. The HCO^+ molecule may not be depleted in an envelope since there is no chemical reaction route to consume it (Rawlings 1996; van Dishoeck & Blake 1998). Moreover, it often delineates well outflow lobes (Hogerheijde et al. 1998; Hogerheijde et al. 1999). Thus it may be a good tracer of the density and motion of the envelope and the outflow. However, since the transition may be opaque, we selected C_3H_2 2_{12}–1_{01} as a complementary probe to cold gas in the envelope. The C_3H_2 molecule has been extensively surveyed toward numerous Galactic objects (Madden et al. 1989; Benson, Caselli, & Myers 1998). The single-peaked line profile of C_3H_2 toward L483 obtained from a single dish observation suggests that the transition is not so optically thick (Myers et al. 1995). Furthermore, in L1157 it is found to trace an envelope mainly and is insensitive to an outflow or shocked region (Bachiller & Pérez Guitérrez 1997). Thus, if a disk-like envelope is embedded in the core of L483, we may be able to discern, by using C_3H_2, rotation and/or radial (inward/outward) motions which are not contaminated by the outflow.

The observation of the L483 was carried out with the 10 elements BIMA interferometer in its C configuration in October and November 1998 in the transitions of HCO^+ 1–0 (89.188523 GHz) and C_3H_2 2_{12}–1_{01} (85.338905 GHz). We configured correlator for HCN 1–0 line (88.631847 GHz) as well, but the HCN data were discarded because of interference in the IF band. System temperatures were typically $150 \sim 500$ K during the observation. Projected baselines range from 1.7 kλ to 23 kλ, and phase center was the position of IRAS 18148-0440, $\alpha(2000) = 18^h17^m29\overset{s}{.}83$ and $\delta(2000) = -4°39'38\overset{''}{.}33$. The phase and pass band were calibrated using 1743-038 and 3C273, respectively. We also made observations of Uranus for flux calibration and the flux of 1743-038 was $1.8 \sim 2.0$ Jy at the time of observation. The IF window with the band width of 12.5 MHz was fed into the 256 channels of the correlator for each transition, resulting in the velocity resolutions of 0.164 km s^{-1} and 0.172 km s^{-1} in the HCO^+ and C_3H_2 transitions, respectively. Continua in both upper and lower side bands were simultaneously observed with a 800 MHz bandwidth in total.

We reduced the data using the MIRIAD package. The data were flagged and Fourier transformed with natural weighting. The resulting dirty map was CLEANed and restored with a Gaussian beam of a FWHM size of $14'' \times 10''$ at position angle $5\overset{\circ}{.}5$ measured from North to East.

In addition, in January 1999, one point observation of HCO^+ 1–0 was undertaken toward the IRAS source using the radome-enclosed 14 meter telescope (beam size = 60″) of Taeduk Radio Astronomy Observatory, Korea. The SIS receiver was used for the frontend and the system temperature was 400 K at the time of observation. The backend was an autocorrelation spectrometer with a 20 KHz or 0.067 km s^{-1} resolution.

3. Results

3.1. Continuum emission at $\lambda = 3.4$ mm

Fig. 1 represents the continuum emission detected around the position of IRAS 18148-0440. There is diffuse emission in the NE–SW direction. The continuum source is barely resolved in the direction of major beam axis, but extended in the E-W direction. By deconvolving the beam, we roughly estimate the size of condensation, 2000 AU and 3000 AU in the N-S and E-W directions, respectively. The estimated total flux is 16 mJy, which is consistent with spectral energy distribution measured from centimeter to near infrared (Fuller et al. 1995). Using a mass absorption coefficient, $\kappa = 0.01(\frac{1.3\mathrm{mm}}{\lambda})^{1.5}$ cm^2 g^{-1} (Motte, André, & Neri 1998), we obtain the mass of 0.13 $M_\odot$ for the condensation.

3.2. C_3H_2 line emission

We illustrate the distribution of C_3H_2 in Fig. 2. The line is single-peaked with the FWHM width of 0.32 km s^{-1} and centered at the systemic velocity of 5.4 km s^{-1}, which is in accordance with the single dish observations of optically thin N_2H^+ and C_3H_2 lines (Myers et al. 1995). The emission peak at $\approx (-9'', -3'')$ is displaced by 6″ to the west of the continuum emission. The C_3H_2 emission is extended from North to South and its half-power contour larger than the synthesized beam is almost circular. From the figure, we note that the C_3H_2 emission delineates the envelope around the protostar fairly well. The single dish observation at high spatial resolution in the $C^{18}O$ 3–2 transition revealed the structure that is similar, but slightly elongated in the N-S direction (Fuller & Ladd 1997).

In order to examine the kinematics of the envelope, we plot channel maps in Fig. 3, where there are mainly three components. The main component at $\approx(-10'', 0'')$ with $v \approx 5.4$ km s^{-1} contains most of the mass of the envelope. The remaining ones are at $\approx(5'', 0'')$ with $v \approx 5.0$ km s^{-1} and at $\approx(15'', 20'')$ with $v \approx 6.0$ km s^{-1}. Extended features in the N–S direction in the figure frame of 5.41 km s^{-1} may result from side lobe effect. The 5.0 and 6.0 km s^{-1} components are minor fragments of the envelope. The systematic displacement of peak positions of the main component along with the LSR velocity suggests a velocity gradient which is seen more clearly in the position-velocity diagrams of Fig. 4. Along the outflow axis of P.A. = 95° (see section

3.3) through the C_3H_2 emission peak at $(-9'', -3'')$, is a uniform velocity gradient of the main component, amounting to ~ 0.5 km s^{-1} over $40''$ or 13 km s^{-1} pc^{-1}. It is found that line wing is of little importance as expected in section 2 and the line *itself* is gradually shifted. The figure also shows that the 5.0 km s^{-1} feature is isolated indeed. On the other hand, the position-velocity diagram across the outflow axis shows little sign of systematic motion. We are not confident with the current resolution that the component at $\Delta\delta \approx -20''$ with 5.6 km s^{-1} is a discrete one.

A plausible explanation of those velocity shifts would be that the envelope has a flattened structure and the velocity gradient represents a gas infall motion toward the central source, whereas the existence of rotation is uncertain (Ohashi et al. 1997). However, one has to be careful since the sense of the velocity shift of infalling flat disk or envelope is always the same as that of outflow motion. For instance, the shift of C_3H_2 line shown in L1228 results from the fragments of core entrained to an outflow (Tafalla & Myers 1997). It is difficult to figure out which one is dominant for L483, given the C_3H_2 data only. However, the velocity shift by outflow is less likely for L483, since the HCO^+ line suggests that there is expanding motion as a part of outflow around the envelope and the velocity field is almost isotropic (see section 4.2). If the C_3H_2 line is affected by this motion, there will be little velocity gradient. Fuller and Wooten (2000) recently found the inward motion by carrying out the VLA observation using the NH_3 inversion lines.

The infall motion of L483 inferred from the position-velocity map of Fig. 4 is different from a free-fall motion of $v(r) = \sqrt{2GM_*/r}$ toward a central star with a mass of M_* which has usually been invoked for, e.g., L1527, HH111, and other YSOs (Ohashi et al. 1997; Yang et al. 1997; Momose et al. 1998). The velocity gradient is rather linear, suggestive of a collapse of a (pressure-free) gas sphere with a uniform density. We would argue that it is not an accretion toward the central source, but a global contraction of the envelope. This is consistent with the current understanding of the class 0 objects (Bachiller 1996). Our interpretation, however, may be subject to the spatial and spectral resolutions of observation. Further observations with higher resolutions are necessary to elucidate the kinematics and structure of the envelope.

3.3. HCO^+ emission

In Fig. 5, we plot the distribution of the red and blue HCO^+ 1–0 wing emission. The red wing is integrated from 6.5 to 11.0 km s^{-1}, while the blue wing from -1.5 to 4.5 km s^{-1}. It is found that the bipolar outflow is well collimated and the peaks of the two outflow lobes are separated each other by $\sim 50''$. The shape of the outflow is similar to those found from CO 2–1 (Parker, Padman, & Scott 1991), from CO 3–2 (Fuller et al. 1995), and from CO 4–3 (Hatchell, Fuller, & Ladd 1999). The outflow lies close to the R.A. axis (P.A.$\approx 95°$). The different amounts of extinction towards the lobes in the IR band suggest an inclination of the outflow of $\sim 45°$ to the sky plane (Fuller et al. 1995).

In order to see details of the outflow, we display channel maps of HCO^+ in Fig. 6. It is found

that there are at least three discrete components in the red shifted outflows: the 5.9 km s^{-1} component around $\approx(35'', 10'')$, the 6.1 km s^{-1} component centered at $\approx(10'', -5'')$, and the 7.2 km s^{-1} component near $\approx(35'', 0'')$. The 7.2 km s^{-1} component spans a wide range of velocity from 6.7 to 10 km s^{-1}. The 5.9 km s^{-1} component is much more widely distributed than the others which are relatively compact. The strong emission around $(-11'', 0'')$ in the velocity range of $5.9 \sim 6.4$ km s^{-1} represents the red side of line core component coming from the envelope. There is little emission in the vicinity of line center ($v = 5.2 \sim 5.7$ km s^{-1}) over the whole field of view, due to heavy self-absorption. The emission on the blue side ($v = 4.5 \sim 5.1$ km s^{-1}) of the systemic component is absent, contrary to the one in the red side (which will be discussed in the next section). Interestingly, the blue outflow lobe also seems to have three discrete components and to share similar kinematics as the red lobe. One can find the 3.3 km s^{-1} component farthest from the systemic velocity, located around $\approx(-10'', 5'')$ whose velocity range is wide from 1.4 to 4.3 km s^{-1}. The other two components have velocities of $\approx$ 4.4 and 5.0 km s^{-1} which reside at $\approx(5'', 5'')$ and $(15'', -10'')$, respectively. The 5.0 km s^{-1} component closest to the rest velocity covers the largest area as the 5.9 km s^{-1} one does in the red lobe.

The fact that the individual velocity components can be identified and grouped into three pairs supports the idea of symmetric and episodic mass ejections. It may be claimed from the number of pairs that the mass loss phenomena have taken place at least three times in the past. There must be an ambient cloud or a cavity wall with velocity close to the systemic one which embeds these different velocity components, but this is probably resolved out, since its distribution would be extended. The shortest baseline mentioned in section 2 suggests that we are blind to structures larger than $\sim 100''$. The clumpiness and intermittency of the outflow is rather common in the case of extreme high velocity outflows (Bachiller 1996). It seems that standard or low velocity outflows exhibit such features as well (cf. Hogerheijde et al. 1998; Gómez et al. 1999).

Furthermore, we note that the component whose velocity is closer to the systemic one occupies larger area. This can be evidence that an opening angle of the outflow becomes wider as the YSO evolves (Bachiller 1996), provided that the ejected material is accelerated after the ejection from around zero velocity. If this assumption holds, then the high velocity component will be located far away from the driving source. Actually the velocity roughly proportional to the distance away from the source is a reasonable approximation to the velocity field of the well-collimated flow, as can be seen in HH211, NGC1333-IRAS2, NGC2071, and NGC2264G (Masson & Chernin 1993; Gueth & Guilloteau; Sandell et al. 1994; Chernin & Masson; Fich & Lada 1998). It is approximately true for the L483 as well, which is shown in the position-velocity diagram of Fig. 7. The velocity increase together with the distance from the source could also be made by other mechanisms like the simultaneous outburst of material with a wide range of velocities. However, this may not be applicable to the well-collimated outflows with narrow throats.

On the other hand, one can imagine that the opening angle has been kept wide from the beginning, but the fastest mass ejection has taken place preferentially normal to the flat disk or envelope. Although this is not the case for the general class 0 objects, this possibility can not

be ruled out. The slowly moving material with wider opening angle could also be regarded as a remnant of a pre-existing shell which was slowly expanding and is swept up by the fast jet. All these invoke detailed understanding of the outflow and hence should be tested by further observation.

4. Discussion

4.1. Abundance estimate of HCO^+ in the outflow

The line strength of HCO^+ in the wings indicates that the molecule may be enhanced in the outflow region. We estimate the column density of HCO^+ and CO in the outflow lobe in order to derive the relative abundance of HCO^+ to CO. Since the line wings are as wide as 5 km s^{-1} along any line of sights, the condition of the *large velocity gradient* is applicable. Then we can use an expression by Goldreich & Kwan (1974):

$$\tau = \frac{8\pi^3\mu^2}{3h}\frac{R}{V}n_0(1-e^{-T_0/T_{\rm ex}}), \tag{1}$$

where $\mu(=3.4\mathrm{debye})$ is the dipole moment of HCO^+, R/V is the velocity gradient, n_0 is the level population in the level $J=0$, $T_{\rm ex}$ is the excitation temperature, and $T_0(=h\nu_{10}/k)$ is 4.2 K. If we use an approximation, $(n_0+n_1+n_2+\cdots)/n_0 \equiv n_t/n_0 \simeq 2kT_{\rm ex}/h\nu_{10}$,

$$\tau = \frac{2\pi^3\mu^2\nu_{10}}{3kT_{\rm ex}V}N(\mathrm{HCO^+})(1-e^{-T_0/T_{\rm ex}}), \tag{2}$$

where the column density $N(HCO^+)$ is equal to $2Rn_t$.

The τ is derived from

$$T_{\rm b} = (J(T_{\rm ex}) - J(2.7K))(1-e^{-\tau}), \tag{3}$$

where $J(T) = T_0/(e^{T_0/T}-1)$. Since $T_{\rm b} \approx 1$ K in the wings (see Fig. 8), $\tau \approx 0.15$ for an assumed $T_{\rm ex}$ of 10 K. $N(HCO^+)$ is then 1.4×10^{13} cm^{-2} for $V=5$ km s^{-1}. In the case that $T_{\rm ex}=20$ K, $\tau \approx 0.051$ and $N(HCO^+) = 1.7\times10^{13}$ cm^{-2}.

We derive the column density of CO in the outflow lobe in a similar way by using the J=2–1 transitions of both ^{12}CO and ^{13}CO in Hatchell, Fuller, & Ladd (1999). The resulting CO column density is $N(\mathrm{CO}) = 4.2\times10^{17}$ cm^{-2}, where we adopted $\tau=4.0$ and $T_{\rm ex}=25$ K. Finally it is found that the abundance of HCO^+ relative to CO is $(3.3\sim4.0)\times10^{-5}$. This is comparable to the value of $\sim10^{-4}$ inferred either for the Orion extended ridge or for the TMC-1 region (Irvine, Goldsmith, & Hjalmarson 1987). Thus we find no significant abundance enhancement of HCO^+ in the outflow. The line wings look rather strong simply due to the depression of the line core.

4.2. Anti-infall signature of the HCO^+ lines

Line profiles of HCO^+ 1–0 toward the envelope are displayed in Fig. 8, where a spectrum obtained toward the IRAS source with the single dish telescope is shown together. Emission from line core is mildly self-absorbed in the single dish observation, but suffers from severe self-absorption in the array observation, falling off close to zero. The self-absorption of the line core is usually amplified in the interferometric observation, since the rest velocity component is most extended and the lack of visibility data at short spacing filters it out. Here it should be pointed out that the blue peak is weaker than the red one in the single dish observation and even almost missing in the interferometric one. This asymmetry is consistent with those of higher transitions of HCO^+ (Gregersen et al. 1997). All these observations strongly suggest that the stronger red peak is not an artifact caused by the limited UV coverage of interferometric observation, but an intrinsic property of the envelope of L483. The stronger red peak of optically thick line is generally known as an *anti-infall* signature, indicative of an outward motion. However, it contradicts the observations of HCN, H_2CO, and NH_3, all implying the inward motion (Park, Kim, & Minh 1999; Myers et al. 1995; Fuller & Wooten 2000).

What gives rise to the anti-infall asymmetry of HCO^+? In answering this question, however, we should not violate observational facts of HCN, H_2CO, and NH_3 supporting the collapse motion. First, we can consider the influence of the outflow. In addition to the self-absorption by the surface layer of the envelope, the blue lobe of the outflow in front of the envelope may further obscure the blue part of line core emission. However, since the outflow will have a higher excitation temperature than the envelope (Hatchell, Fuller, & Ladd 1999), it makes the emission from the envelope brighter irrespective of its optical depth: if the outflow is optically thin, the emission from the outflow should be added to that of envelope, while if the outflow is opaque, then the emission from outflow will replace it. Therefore the outflow can not explain the anti-infall asymmetry of the line core.

The asymmetry seems to arise from the envelope itself or very close to it. The envelope or material in its vicinity may be really in a state of almost isotropic expansion. Here we recall that the material (traced by HCO^+) whose velocity is close to the systemic one moves outward with a wide opening angle, whereas the envelope (traced by C_3H_2) is collapsing. Thus one viable option may be a nearly isotropic outward motion of gas between the disk-like envelope and the collimated outflow, which is actually a part of the outflow. If this motion takes place over a large amount of volume around the flattened envelope, then we will have line profiles with the anti-infall signature. The detail of the line shape depends on the velocity field in this expanding volume, but in any case the line will have the red peak stronger than the blue (Leung 1978). To summarize, there is a highly collimated jet-like flow far from the central source, while there is a wide angle wind-like mass ejection at the base of the outflow. Therefore the geometry and kinematics of the outflow of L483 seems to be in favor of the X-wind model as a low velocity version (cf. Bachiller 1996; Li & Shu 1996). The Cep A-HW2 is one of the recent examples showing similar line shapes as L483 (Gómez et al. 1999).

Then one may have to look for reason why only the HCO^+ reflects the expansion. This could be explained in terms of its abundance and excitation condition. The main route to form HCO^+ is the reaction between H_3^+ and CO. The HCO^+ is unlikely to be depleted, since both species are abundant in the quiescent and relatively diffuse clouds (van Dishoeck & Blake 1998; Langer, Velusamy, & Xie 1996). As a consequence, although HCO^+ has a large critical density, it is collisionally excited easily at lower densities due to the line trapping. In this case, the critical density, n_c, should be modified as $A_{ji}/(C_{ji}\tau_{ji})$, where τ_{ji} is an optical depth, as already pointed out by Genzel (1991). It is also shown with a simple LVG analysis that HCO^+ 1–0 transition requires the lowest effective density, n_{eff}, among CS, H_2CO, HCN, and HCO^+ to produce the line intensity of 1 K for a given column density per unit velocity interval of $\log(N/\Delta V) = 13.5$, where the column density, N, is given in cm^{-2} and the line width, ΔV, in km s^{-1} (Evans 1999). (At $T_k = 10$ K, $n_{eff} = 2.4 \times 10^3$ cm^{-3} for HCO^+ 1–0, while $n_{eff} = 1.8 \times 10^4$, 6.0×10^4, and 2.9×10^4 cm^{-3}, for CS 2–1, H_2CO 2_{12}–1_{11}, and HCN 1–0, respectively.) Thus the expanding part of the envelope could be more effectively traced by the HCO^+ 1–0 transition than by other transitions. Park, Kim, and Minh (1999) compared the line profiles of HCO^+ 3–2 & 4–3, H_2CO 2_{12}–1_{11}, CS 2–1, and HCN 1–0 of 9 class 0 and I objects, and found that the HCO^+ molecule seems to prefer the anti-infall asymmetry than the HCN and possibly the CS does. The preference is very marginal due to a small number of samples, but this could be indirect evidence supporting the idea mentioned above.

4.3. Position of the young stellar object in L483

As shown in Fig. 1, the position of continuum peak coincides with that of IRAS 18148-0440 within $2'' \sim 3''$, while the peak of C_3H_2 emission is displaced to the west by $6''$ from it. Although HCO^+ is severely saturated, the emission peak of the red part of the systemic component at $v \approx 5.9$ km s^{-1} is roughly coincident with that of C_3H_2, as represented in Fig. 6.

Are the two sources really different condensations? The error ellipse of the IRAS source position is as large as $35'' \times 8''$ with a position angle of 86° (IRAS Point Source Catalogue). However, it is found from the VLA observation that the 3.6 cm and 6 cm continuum source is detected exactly at the IRAS position and there is no emission at the position of the C_3H_2 emission peak. Although the VLA beam is $19'' \times 9''$ and $10'' \times 5''$ at 3.6 cm and 6 cm, respectively, the accuracy in determining the peak position should be better than $1'' \sim 2''$ (Anglada, Sepúlveda, & Gómez 1997; Anglada et al. 2000; Beltrán et al. 2000). The far-infrared ($100 \sim 190\mu$m) and submillimeter ($450 \sim 1100\mu$m) continuum emission are also detected at the IRAS source position, but the beams are as large as $\approx 50''$ and $\approx 20''$, respectively (Fuller et al. 1995; Ladd et al. 1991). Recently Fuller and Wooten (2000) mapped the region at $\lambda = 450$ and $850\mu m$ and found an elongated condensation at the IRAS position with P.A. $\approx 70°$ whose (beam-convolved) FWHM size is $\approx 30'' \times 15''$. Thus there may be an object at $\approx (-9'', -3'')$ which is unveiled only in millimeter line emission and possibly in the continuum from sub-millimeter to far-infrared.

However, it is more likely that the line emission of C_3H_2 and HCO^+ and the continuum emission emanate from the same condensation but that the molecular line emission is depressed around the dust condensation by some reasons. One of the reasons may be that the gas is frozen out onto the grain in the cold and dense environment. One can find such examples in VLA 1623 and NGC 2024 (André, Ward-Thompson, & Barsony 1993).

5. Summary

The BIMA array observation has been undertaken toward the IRAS 18148-0440, a YSO embedded in the L483 molecular core. An envelope with a beam-deconvolved size of $\sim$ 3000 AU (R.A.) $\times$ 2000 AU (Dec.) and with a mass of $\sim 0.13 M_\odot$ is found to collapse towards its center. The collapse motion is different from the Shu type ($v \propto r^{-1/2}$), but more likely linear with a velocity gradient of $\sim$ 13 km s^{-1} pc^{-1}. The YSO seems to undergo main accretion phase without any conclusive signature of rotation. The molecular outflow traced by HCO^+ 1–0 suggests that there have been successive (at least three times) mass loss events to date and that the recent ejection might take place with a wide opening angle compared with previous ones. The rest velocity component of the HCO^+ line is found to exhibit the anti-infall signature, while the other transitions of density tracing molecules like CS, H_2CO, and HCN are not. If the outflow is poorly collimated at its base, the outward motion directed radially would be pervasive in both sides of the flattened envelope and responsible for the HCO^+ 1–0 line biased to the red. Due to the ease of collisional excitation and little chance of depletion, the HCO^+ 1–0 is the most likely transition with which one can sense the outward motion.

We thank the anonymous referee for his careful reading of the manuscript. YSP was partially supported by the BK21 program of Ministry of Education, Korea.

REFERENCES

André, P., Ward-Thompson, D., Barsony, M., 1993, ApJ, 406, 122

Anglada, G., Rodrígez, L.F., Cantó, J., Estalella, R., López, R., 1987, A&A, 186, 280

Anglada, G., Sepúlveda, I., Gómez, J.F., 1997, A&AS, 121, 255

Anglada et al., 2000, in preparation

Bachiller, R., 1996, ARAA, 34, 111

Bachiller, R., Pérez Guitérrez, M., 1997, ApJ, 487, L93

Beltrán et al., 2000, in preparation

Benson, P.J., Caselli, P., Myers, P.C., 1998, ApJ, 506, 743

Buckle, J.V., Hatchell, J., Fuller, G.A., 1999, A&A, 348, 584

Chernin, L.M., Masson, C.R., 1992, ApJL, 396, 35

Choi, M., Panis, J.-F., Evans, N.J.II, 1999, ApJ, 122, 519

Evans, N.J.II, 1999, ARAA, 37, 311

Fich, M., Lada, C.J., 1998, ApJS, 117, 147

Fuller, G.A., Lada, E.A., Masson, C.R., Myers, P.C., 1995, ApJ, 453, 754.

Fuller, G.A., Ladd, E.F., 1997, IAU Symp. No. 182, Herbig-Haro Flows and the Birth of Low Mass Stars, eds. B. Reipurth and C. Bertout (Kluwer: Netherlands), p.495

Fuller, G.A., Myers, P.C., 1993, ApJ, 418, 273

Fuller, G.A., Wooten, A., 2000, ApJ, in press

Genzel, R., 1991, Chemistry in Space, eds. J.M. Greenberg and V. Pirronello (Kluwer: Netherland), p. 123

Goldreich, P., Kwan, J., 1974, ApJ, 189, 441

Gómez, J.F., Sargent, A.I., Torelles, J.M., Ho, P.T.P., Rodríguez, L.F., Cantó, J., Garay, G., 1999, ApJ, 514, 287

Gregersen, E.M., Evans, N.J.II, Zhou, S., Choi, M., 1997, ApJ, 484, 256

Gueth, F., Guilloteau, S., 1999, A&A, 343, 571

Hatchell, J., Fuller, G.A., Ladd, E.F., 1999, A&A, 346, 278

Hogerheijde, M.R., van Dishoeck, E.F., Blake, G.A., van Langevelde, H.J., 1998, ApJ, 502, 315

Hogerheijde, M.R., van Dishoeck, E.F., Salverda, J.M., Blake, G.A., 1999, ApJ, 513, 350

Irvine, W.M., Goldsmith, P.F., Hjalmarson, Å, 1987, IAU Symp. No. 120, Interstellar Processes, eds. D.J. Hollenbach and H.A., Thronson (Dordrecht: Reidel), p. 561

Kitamura, Y., Saito, M., Kawabe, R., Sunada, K., 1997, IAU Symp. No. 182, Herbig-Haro Flows and the Birth of Low Mass Stars, eds. B. Reipurth and C. Bertout, (Kluwer: Netherland), p. 381

Ladd, E.F., Adams, F.C., Casey, S., Davidson, J.A., Fuller, G.A., Harper, D.A., Myers, P.C., Padman, R., 1991, ApJ, 366, 203

Langer, W.D., Velusamy, T., Xie, T., 1996, ApJ, 468, L41

Leung, C.M., 1978, ApJ, 427, 441

Leung, C.M., Brown, R.L., 1977, ApJL, 214, L73

Li, Z.-Y., Shu, F.H., 1996, ApJ, 468, 261

Madden, S.C., Irvine, W.M., Matthews, H.E., Friberg, P., Swade, D.A., 1989, AJ, 97, 1403

Mardones, D., 1998, Ph.D. thesis, Harvard University

Mardones, D., Myers, P.C., Tafalla, M., Wilner, D.J., Bachiller, R., Garay, G., 1997, ApJ, 489, 719

Masson, C.R., Chernin, L.M., 1993, ApJ, 414, 230

Momose, M., Ohashi, N., Kawabe, R., Nakano, T., Hayashi, M., 1998, ApJ, 504, 314

Motte, F., André, P., & Neri, R., 1998, A&A, 336, 150

Myers, P.C., Bachiller, R., Caselli, P., Fuller, G.A., Mardones, D., Tafalla, M., Wilner, D.J., 1995, ApJ, 449, L65

Ohashi, N., Hayashi, M., Ho, P.T.P., Momose, M., 1997, ApJ, 475, 211

Park, Y.-S., Kim, J., Minh, Y.C., 1999, ApJ, 520, 223

Parker, N.D., Padman, R., Scott, P.F., 1991, MNRAS, 252, 442

Rawlings, J.M., 1996, ApSS, 237, 299

Sandell, G., Knee, L.B.G., Aspin, C., Robson, I.E., Russell, A.P.G., 1994, ApJL, 285, 1

Tafalla, M., Myers, P.C., 1997, ApJ, 491, 653

van Dishoeck, F.F., Blake, G.A., 1998, ARAA, 36, 317

Yang, J., Ohashi, N., Yan, J., Liu, C., Kaifu, N., Kimura, H., 1997, ApJ, 475, 683

Zhou, S., Evans, N.J.II., Kömpe, C., Walmsley, C.M., 1993, ApJ, 404, 232

This preprint was prepared with the AAS LaTeX macros v4.0.

Fig. 1.— Map of continuum emission at $\lambda = 3.4$ mm. Contour levels are from $\pm 2\sigma$ in steps of 1.5σ, where $1\sigma = 0.8$ mJy beam^{-1}. The position of IRAS 18148-0440 or the phase center is marked with a cross at $\alpha(2000) = 18^h17^m29\overset{s}{.}83$ and $\delta(2000) = -4°39'38\overset{''}{.}33$. The synthesized beam is shown in the bottom left.

Fig. 2.— Map of the C_3H_2 intensity integrated from 4.5 to 6.5 km s^{-1}. Contour levels start at $\pm 2\sigma$ with an increment of 1.5σ, where $1\sigma = 0.1$ Jy beam^{-1} km s^{-1}

Fig. 3.— Channel maps of C_3H_2. Contour levels are from $\pm 4\sigma$ with an increment of 4σ, where $1\sigma = 0.1$ Jy beam^{-1}. The LSR velocities are designated in the upper left corner of each figure frame.

Fig. 4.— Position-velocity diagram of C_3H_2 along the outflow axis (left) and perpendicular to it (right). Contour levels are from 4σ by an increment of 4σ, where $1\sigma = 0.11$ K. Beam size and spectral resolution are indicated in the bottom left of each panel.

Fig. 5.— Integrated intensity map of blue (solid contour) and red (dashed contour) wings of the HCO^+ line superimposed on the continuum map (grey). The blue wing is integrated from -1.5 to 4.5 km s^{-1} and the red wing from 6.5 to 11.0 km s^{-1}. Both the lowest contour and the increment step are 5σ for both wings, where $1\sigma = 0.1$ Jy beam^{-1} km s^{-1}.

Fig. 6.— Channel maps of HCO^+. Contour levels are from $\pm 5\sigma$ Jy beam^{-1} by an increment of 5σ Jy beam^{-1}, where $1\sigma = 0.1$ Jy beam^{-1}. The LSR velocities are designated in the upper left corner of each figure frame. Note that 3 frames between the LSR velocities of 5.10 and 5.76 km s^{-1} are skipped since they show little emission due to the heavy self-absorption.

Fig. 7.— Position-velocity diagram of HCO^+ along the outflow axis (P.A. = 95°) through the (0,0) position. Contour levels are at 3σ intervals from 5σ, where $1\sigma = 0.11$ K. Beam size and spectral resolution are indicated in the bottom left.

Fig. 8.— Line profiles of HCO^+ from the array (left) and the single dish (right) observations towards the envelope. Offsets from the IRAS source position are shown in the upper left corner of each panel for the interferometer observation.

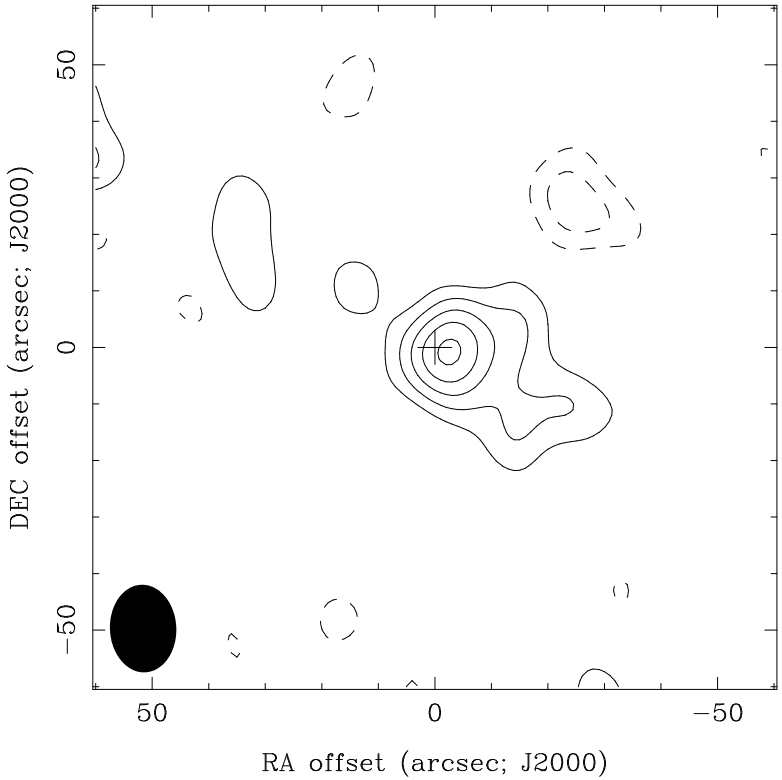
50
0
−50
DEC offset (arcsec; J2000)
50
0
−50
RA offset (arcsec; J2000)

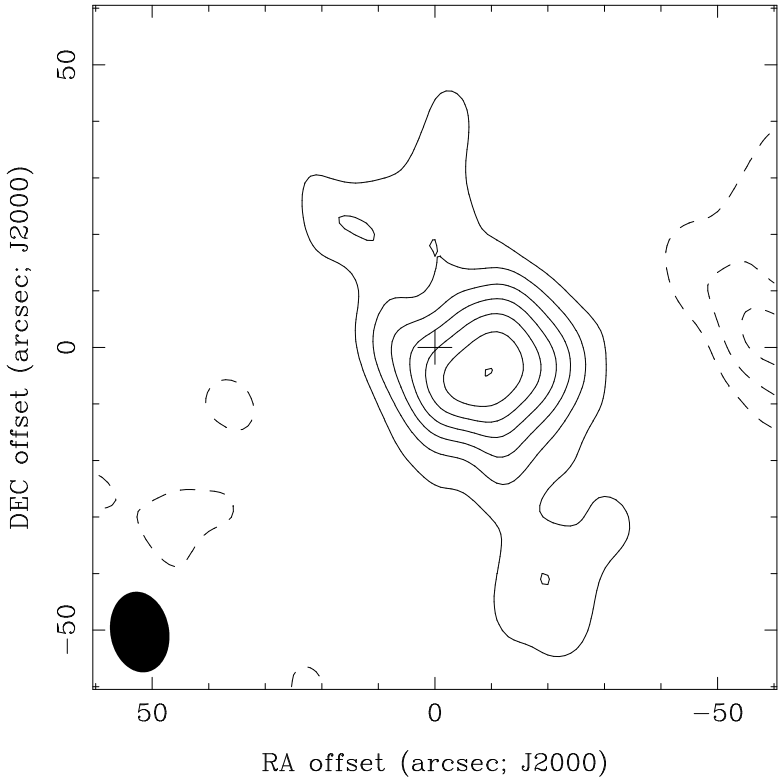
50
0
−50
DEC offset (arcsec; J2000)
50
0
−50
RA offset (arcsec; J2000)

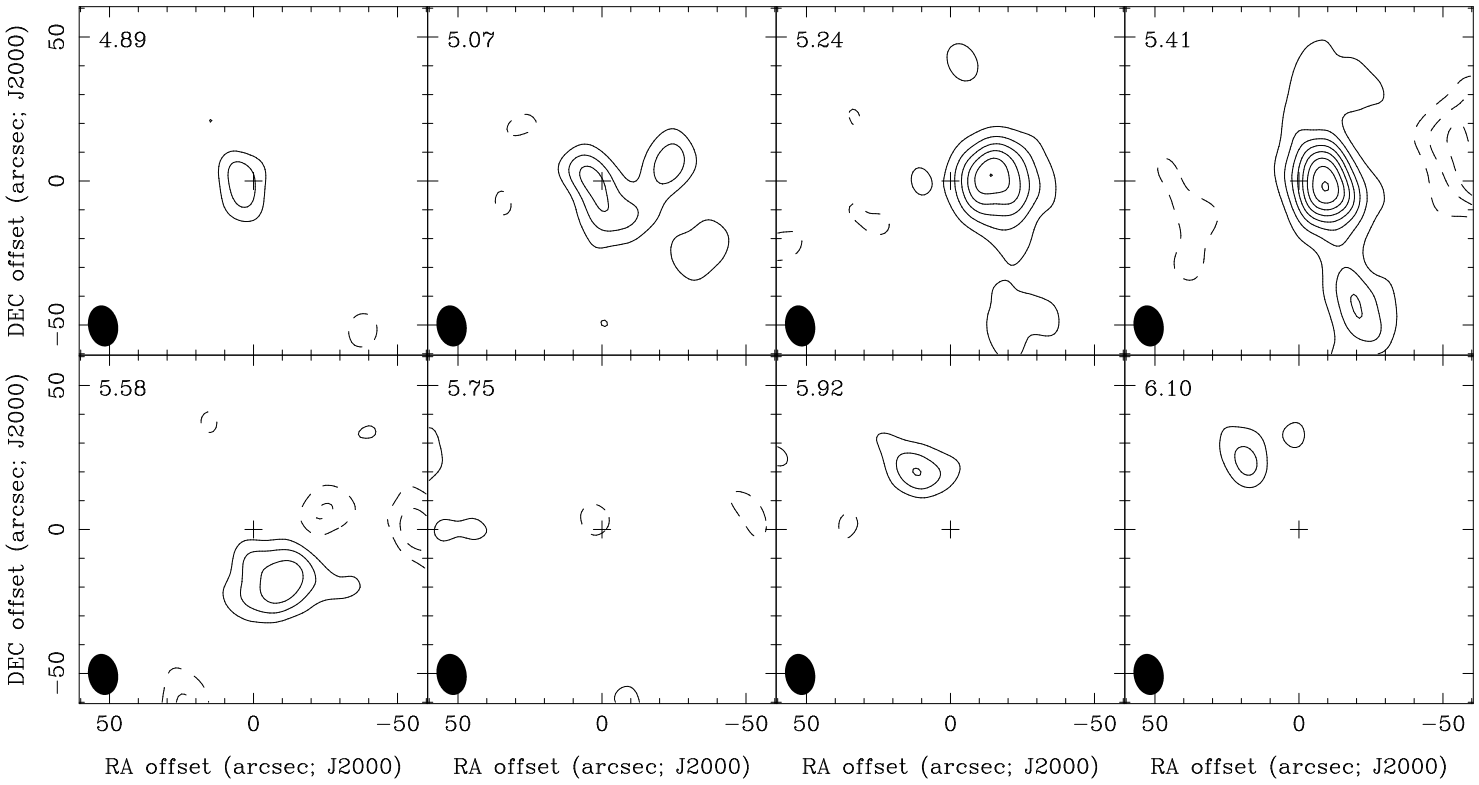
4.89
5.07
5.24
5.41
5.58
5.75
5.92
6.10
DEC offset (arcsec; J2000)
RA offset (arcsec; J2000)
50
0
−50

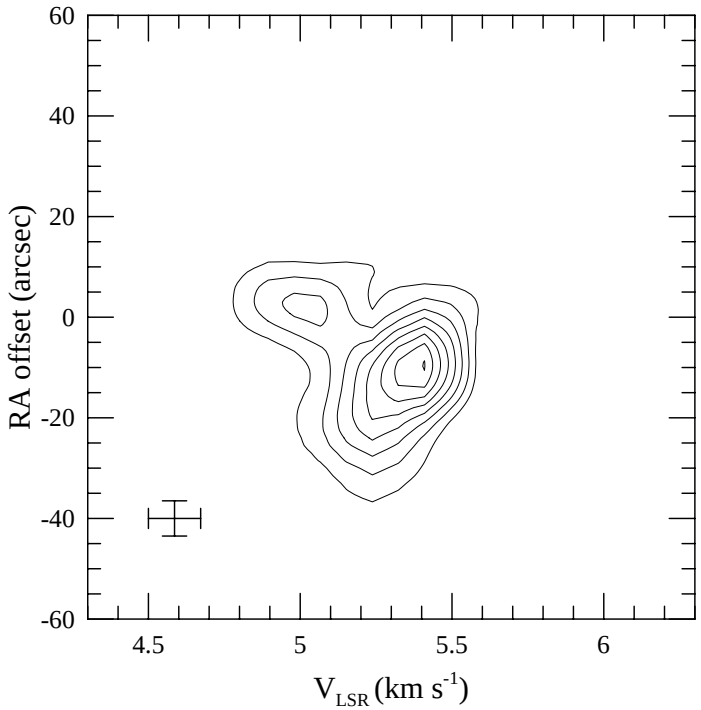
60
40
20
0
-20
-40
-60
RA offset (arcsec)
4.5
5
5.5
6
V_LSR (km s^-1)

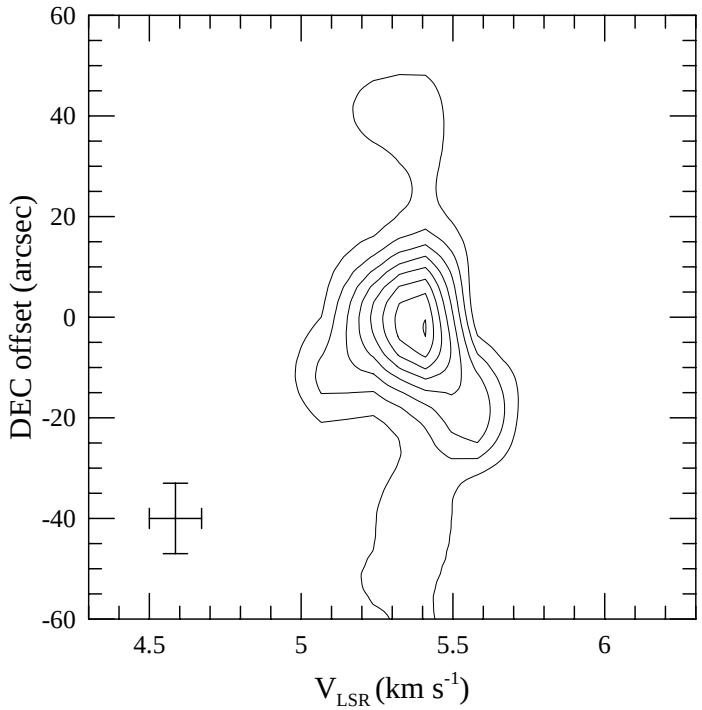
60
40
20
0
-20
-40
-60
DEC offset (arcsec)
4.5
5
5.5
6
V_LSR (km s^-1)

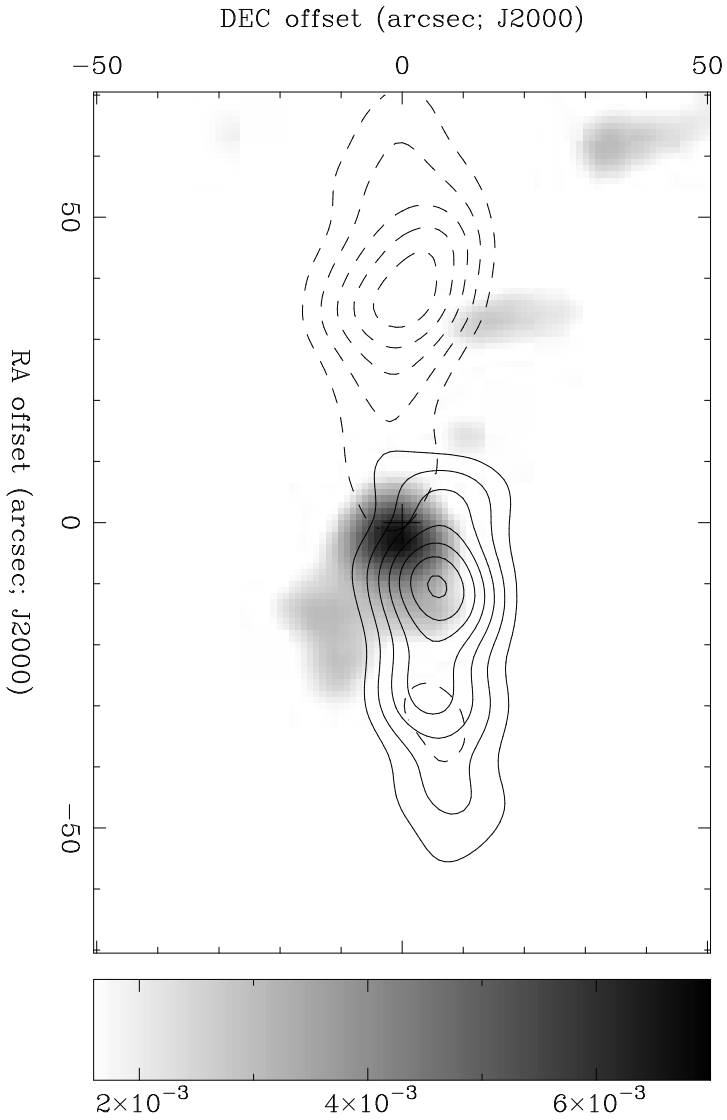
DEC offset (arcsec; J2000)
−50
0
50
RA offset (arcsec; J2000)
50
0
−50
2×10−3
4×10−3
6×10−3

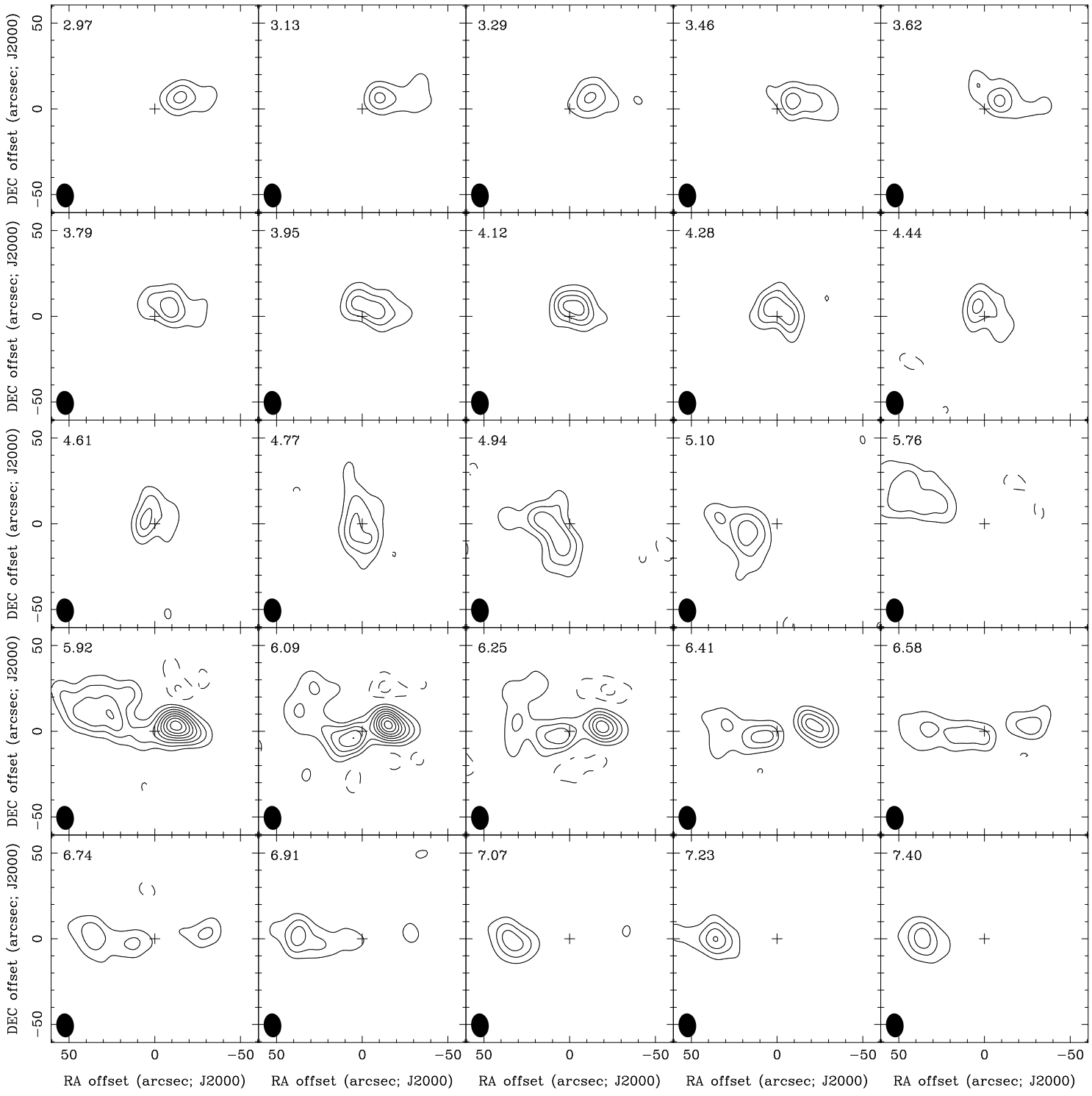
2.97
3.13
3.29
3.46
3.62
3.79
3.95
4.12
4.28
4.44
4.61
4.77
4.94
5.10
5.76
5.92
6.09
6.25
6.41
6.58
6.74
6.91
7.07
7.23
7.40
DEC offset (arcsec; J2000)
RA offset (arcsec; J2000)
50
0
−50

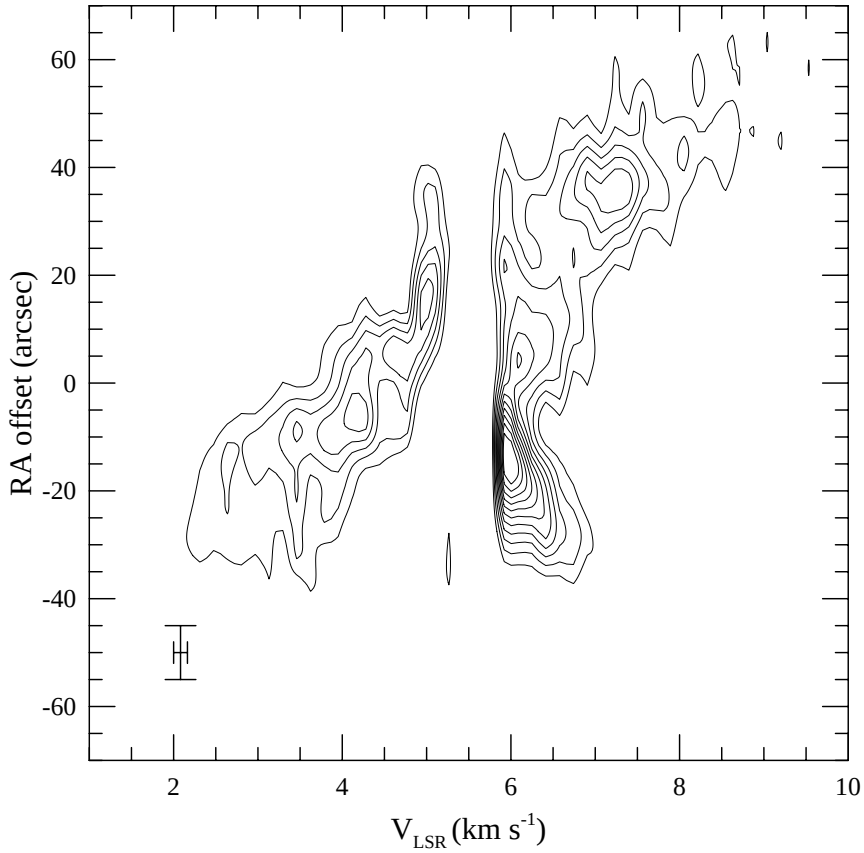
60
40
20
0
-20
-40
-60
RA offset (arcsec)
2
4
6
8
10
V_LSR (km s^-1)

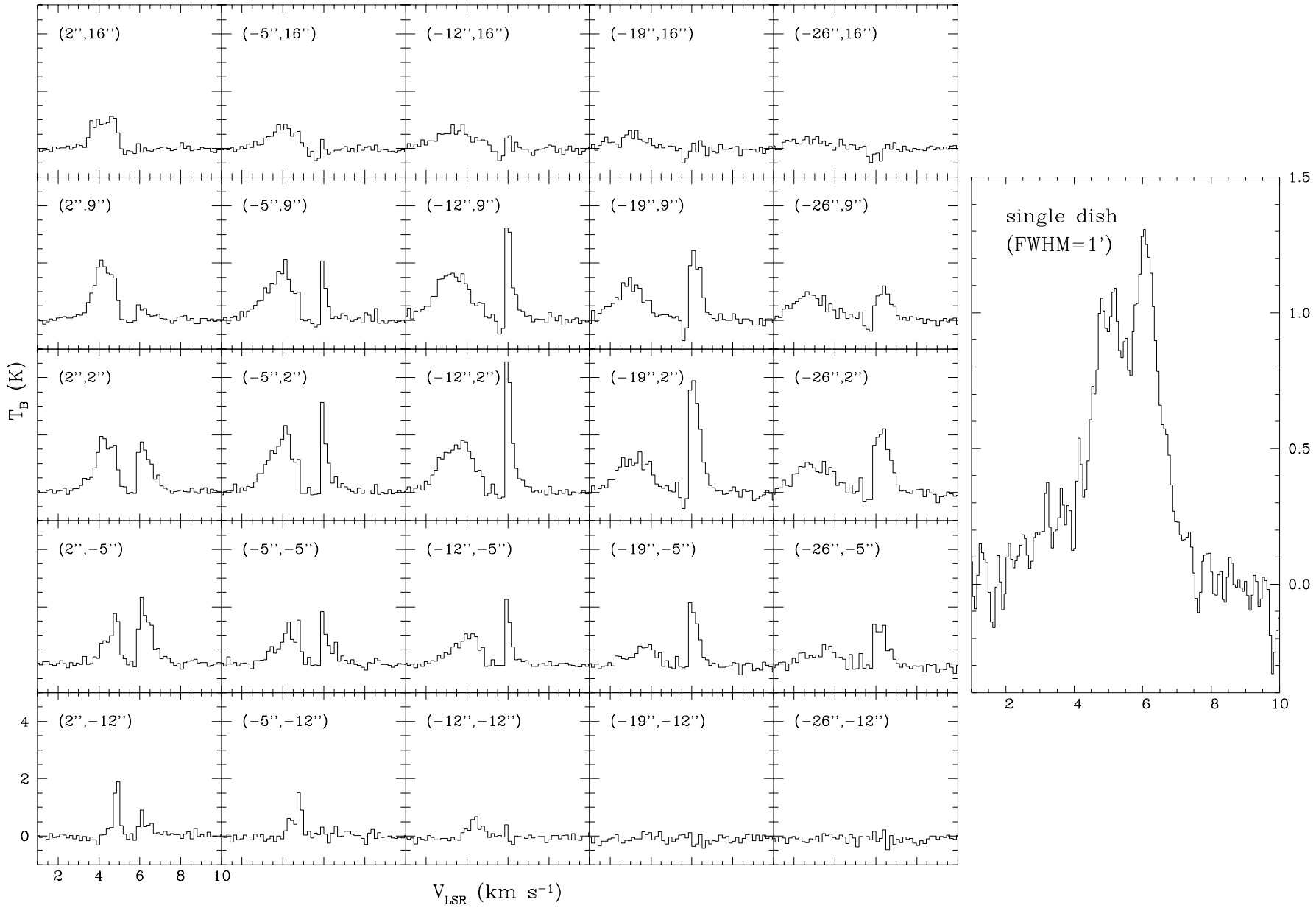
(2'',16'')
(−5'',16'')
(−12'',16'')
(−19'',16'')
(−26'',16'')
(2'',9'')
(−5'',9'')
(−12'',9'')
(−19'',9'')
(−26'',9'')
(2'',2'')
(−5'',2'')
(−12'',2'')
(−19'',2'')
(−26'',2'')
(2'',−5'')
(−5'',−5'')
(−12'',−5'')
(−19'',−5'')
(−26'',−5'')
(2'',−12'')
(−5'',−12'')
(−12'',−12'')
(−19'',−12'')
(−26'',−12'')
T_B (K)
V_{LSR} (km s^{-1})
single dish
(FWHM=1')